A Lyapunov-Based Generalized Dc-Side Controller Design for PV-Connected Systems

Preprint

Rahul Mallik,[1] Branko Majmunovic,[2] Soham Dutta,[1]
Gab-Su Seo,[3] Dragan Maksimovic,[2] and Brian Johnson[1]

1 University of Washington
2 University of Colorado
3 National Renewable Energy Laboratory

Presented at the IEEE Energy Conversion Congress and Exposition
Detroit, Michigan
October 9-13, 2022

NREL is a national laboratory of the U.S. Department of Energy
Office of Energy Efficiency & Renewable Energy
Operated by the Alliance for Sustainable Energy, LLC

This report is available at no cost from the National Renewable Energy Laboratory (NREL) at www.nrel.gov/publications.

Contract No. DE-AC36-08GO28308

Conference Paper
NREL/CP-5D00-83961
October 2022

A Lyapunov-Based Generalized Dc-Side Controller Design for PV-Connected Systems

Preprint

Rahul Mallik,[1] Branko Majmunovic,[2] Soham Dutta,[1]
Gab-Su Seo,[3] Dragan Maksimovic,[2] and Brian Johnson[1]

1 University of Washington
2 University of Colorado
3 National Renewable Energy Laboratory

Suggested Citation
Mallik, Rahul, Branko Majmunovic, Soham Dutta, Gab-Su Seo, Dragan Maksimovic, and Brian Johnson. 2022. *A Lyapunov-Based Generalized Dc-Side Controller Design for PV-Connected Systems: Preprint*. Golden, CO: National Renewable Energy Laboratory. NREL/CP-5D00-83961. https://www.nrel.gov/docs/fy23osti/83961.pdf.

© 2022 IEEE. Personal use of this material is permitted. Permission from IEEE must be obtained for all other uses, in any current or future media, including reprinting/republishing this material for advertising or promotional purposes, creating new collective works, for resale or redistribution to servers or lists, or reuse of any copyrighted component of this work in other works.

NREL is a national laboratory of the U.S. Department of Energy
Office of Energy Efficiency & Renewable Energy
Operated by the Alliance for Sustainable Energy, LLC

This report is available at no cost from the National Renewable Energy Laboratory (NREL) at www.nrel.gov/publications.

Contract No. DE-AC36-08GO28308

Conference Paper
NREL/CP-5D00-83961
October 2022

National Renewable Energy Laboratory
15013 Denver West Parkway
Golden, CO 80401
303-275-3000 • www.nrel.gov

NOTICE

This work was authored in part by the National Renewable Energy Laboratory, operated by Alliance for Sustainable Energy, LLC, for the U.S. Department of Energy (DOE) under Contract No. DE-AC36-08GO28308. Funding provided by U. S. Department of Energy Office of Energy Efficiency and Renewable Energy Solar Energy Technologies Office, grant numbers DE-EE0009025 and DE-EE0008346, the Washington Research Foundation, and the National Science Foundation through grant 1509277 is gratefully acknowledged. The views expressed herein do not necessarily represent the views of the DOE or the U.S. Government. The U.S. Government retains and the publisher, by accepting the article for publication, acknowledges that the U.S. Government retains a nonexclusive, paid-up, irrevocable, worldwide license to publish or reproduce the published form of this work, or allow others to do so, for U.S. Government purposes.

This report is available at no cost from the National Renewable Energy Laboratory (NREL) at www.nrel.gov/publications.

U.S. Department of Energy (DOE) reports produced after 1991 and a growing number of pre-1991 documents are available free via www.OSTI.gov.

Cover Photos by Dennis Schroeder: (clockwise, left to right) NREL 51934, NREL 45897, NREL 42160, NREL 45891, NREL 48097, NREL 46526.

NREL prints on paper that contains recycled content.

A Lyapunov-based Generalized Dc-Side Controller Design for PV-Connected Systems

R. Mallik*, B. Majmunovic†, S. Dutta*, G.-S. Seo‡, D. Maksimovic†, and B. Johnson*
*Department of Electrical and Computer Engineering, University of Washington, Seattle, WA 98195, USA
Email: rmallik@uw.edu, sdutta@uw.edu, brianbj@uw.edu
† Department of Electrical, Computer, and Energy Engineering, University of Colorado, Boulder, CO 80309, USA
Email: branko.majmunovic@colorado.edu, maksimov@colorado.edu
‡Power Systems Engineering Center, National Renewable Energy Laboratory, Golden, CO 80401, USA
Email: gabsu.seo@nrel.gov

***Abstract*—The objective of this paper is to realize a universal dc-side controller for photovoltaic (PV) systems where the control is agnostic to the downstream converter configuration. To achieve this, the downstream power converter and its controls are manipulated into an effective power control loop that is then cast into a generalized multi-loop design framework. On the dc side, a nonlinear small-signal model of the PV input is realized exclusively in terms of PV datasheet parameters (i.e., open-circuit voltage, short-circuit current, and maximum power point). Finally, a linear controller is used to modulate the dc-side PV system with the generic downstream power controller. A Lyapunov candidate is proposed to analyze the stability of the interconnected system and provide a streamlined approach for the controller design. The proposed design is validated on a 1 kVA experimental setup that interfaces a PV module to the grid.**

I. Introduction

Design of generic dc-side controls in grid-connected photovoltaic (PV) systems is impeded by the wide range of converter topologies that may appear on the downstream dc-ac conversion stage [1]. In this paper, we focus on developing a generalized dc-side controller that is agnostic to the dc-ac converter topology and its control. Toward that end, we manipulate everything downstream to the PV module into an effective power control loop that interacts with the maximum power point tracker (MPPT) and the PV dc-link control such that stable and robust power dispatch are realized. The primary focus of this paper is to propose a systematic design procedure for the PV dc-link controller. Our approach leverages the Lyapunov theory to analyze the stability of the interconnected system and provide closed-form expressions of the controller gains that are universally applicable to any PV-connected system.

Funding provided by U. S. Department of Energy Office of Energy Efficiency and Renewable Energy Solar Energy Technologies Office, grant numbers DE-EE0009025 and DE-EE0008346, the Washington Research Foundation, and the National Science Foundation through grant 1509277 is gratefully acknowledged. This work was authored in part by Alliance for Sustainable Energy, LLC, the manager and operator of the National Renewable Energy Laboratory for the U.S. Department of Energy (DOE) under Contract No. DE-AC36-08GO28308. The views expressed in the article do not necessarily represent the views of the DOE or the U.S. Government. The U.S. Government retains and the publisher, by accepting the article for publication, acknowledges that the U.S. Government retains a nonexclusive, paid-up, irrevocable, worldwide license to publish or reproduce the published form of this work, or allow others to do so, for U.S. Government purposes.

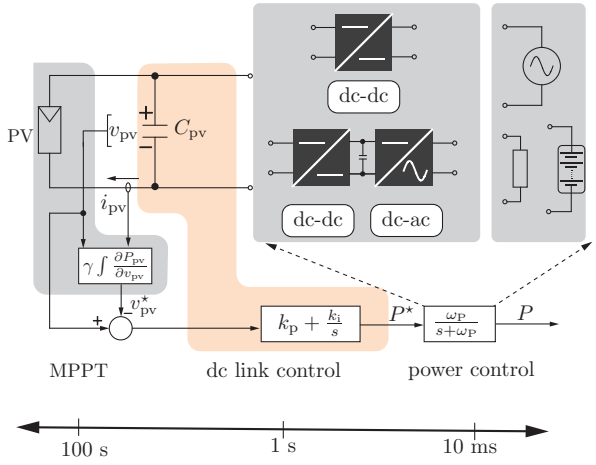

Fig. 1: Generalized control loop structure for a PV system and its converter(s). The entire downstream converter and control are encapsulated into an equivalent first order transfer function whose effective bandwidth is $\omega_{\rm P}$. For this paper we focus exclusively on the highlighted dc-link control.

Accurate modeling of PV is essential to capture the instabilities that can appear when interacting with the other loops in the system. Existing PV modeling approaches [2] typically depend on knowledge of physics-based parameters which often need extensive experimentation to characterize. This is avoided in [3] by linearizing the PV model around the maximum power point (MPP) such that only the MPP voltage and current are needed. However, we will show that such models fail to predict instabilities that arise when oscillations around the MPP are sufficiently large.

To capture the fidelity of the small-signal model throughout the PV operation from open-circuit to short-circuit condition, the notion of PV dynamic resistance, which we denote as $r_{\rm pv}$, was first proposed and experimentally validated in [4]. Existing linear small-signal impedance models of dc-dc converters [5], [6] and inverters [7], [8] were eventually modified to include PV dynamic resistance. Similarly, the concept of dynamic resistance was extended to dc-dc converters [9] and inverters [10] in the state-space formulation. These ap-

This report is available at no cost from the National Renewable Energy Laboratory at www.nrel.gov/publications.

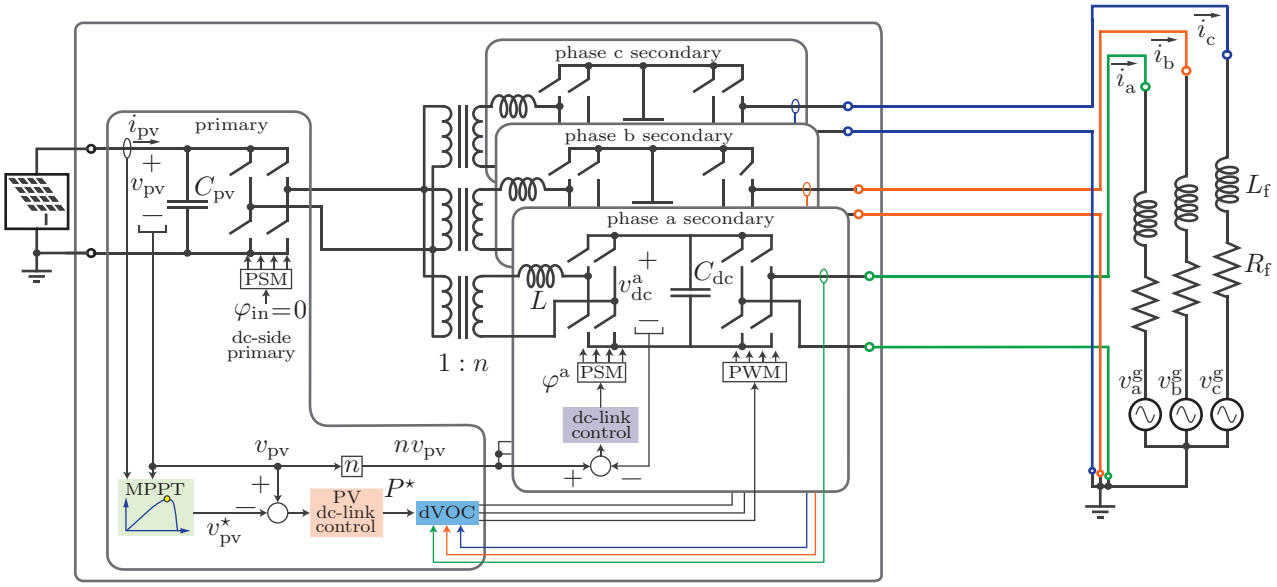

Fig. 2: The multi-stage converter architecture above will serve as a case study for our approach. The converter module comprises three isolated dual-active bridges that each have an ac-side single-phase inverter that interfaces with an ac grid. The various interacting control loops within the converter are shown.

proaches generate transfer functions [7] and state-transition matrices [10] which are heavily dependent on the converter topology and its parameters. This method resulted in an iterative design procedure which sought stable phase margin values and negative eigenvalues. Additionally, the small-signal impedance in these models are obtained experimentally [4] and may change among different PV panels. To circumvent this, we obtain a new PV dynamic resistance that relies exclusively on the parameters provided in PV datasheets. Namely, we utilize the open-circuit voltage, V_{oc}, short-circuit current, I_{sc}, maximum power point voltage, V_{mpp} and maximum power point current, I_{mpp}. This new small-signal model compared to [3] is shown to be valid across all operating points of the PV curve. Moreover, experimental characterization is unnecessary as in [4].

With an accurate PV model and the downstream power control loop designed appropriately, we next design a generalized PV dc-link controller that is agnostic to the downstream converter topology. Sandwiched between the slower MPPT control and the faster power control loop, the design of the generalized PV dc-link controller now becomes a multi-loop control design problem. Conventionally, such problems have been tackled by separating the control subsystems shown in Fig.1 by their respective bandwidths where we design outer loops to be slower and the inner loops to be faster. As the final contribution of this paper we identify shortcomings of timescale-separation-based design methods when applied to the PV model [3]. We then implement a Lyapunov candidate to analyse stability of the dc-link controller. We show that the Lyapunov-based design approach uncovers new and non-trivial conditions that are critical to modeling system stability.

The rest of the paper is organized as follows: Section II gives an overview of the system dynamics and describes the MPPT and the power control loop. Modeling, control design, and Lyapunov-based stability conditions for the dc-link controller are presented in Section III. Claims are verified with experimental results in Section IV.

II. System Description and Dynamics

In this section, we outline the PV system and its control structure.

A. System Architecture

We consider a PV module interfacing with a downstream power electronic converter that is responsible for transfer of energy from the PV to a variety of output resources like grid, battery, or standalone loads. The MPPT controller, PV dc-link controller, and power controller in Fig. 1 work within their own respective timescales to ensure stable operation.

The MPPT controller measures the PV voltage and current to compute the reference voltage, $v_{pv}^{\star}$, for the PV dc-link controller which in turn generates the active power reference $P^{\star}$ for the power converter. As the faster power controller rapidly extracts $P^{\star}$ power from the PV module, the PV voltage, v_{pv}, closely matches the reference, $v_{pv}^{\star}$. Finally, as the MPPT controller slowly nudges $v_{pv}^{\star}$ to the maximum power point voltage, V_{mpp}, the downstream power converter is able to extract the maximum power from the PV.

B. Converter Description

Although the proposed PV modeling and controller design is agnostic to the downstream converter and control, we consider a two-stage converter shown in Fig. 2 for our present analysis. Fig. 2 shows a dual-active bridge based isolated dc-dc stage that connects to the grid through three single-phase inverters. The different hardware stages and associated control loops are described next.

1) Dc-dc Quadruple Active Bridge: We consider a quadruple active-bridge (QAB) based converter [11] connected to the PV module in Fig. 2. The isolated dc-dc stage is formed by three identical dual-active bridge converters that share a primary H-bridge connected to the PV module. Three $1:n$ transformers provides high-frequency isolation between the

This report is available at no cost from the National Renewable Energy Laboratory at www.nrel.gov/publications.

primary and each of the three secondary bridges. All four H-bridges of the QAB are modulated with 50% duty ratio. The phase shift, $\varphi = [\varphi_a, \varphi_b, \varphi_c]^\top$, between the primary bridge and each of the secondary bridge is modulated to ensure each of the floating dc-link voltages, $v_{\rm dc} = [v^a_{\rm dc}, v^b_{\rm dc}, v^c_{\rm dc}]^\top$, are regulated to track n times the input voltage, $v_{\rm pv}$. For each of the three phases, $j \in \{a, b, c\}$, the phase shifts are generated by respective proportional-integral (PI) controllers as follows:

$$\varphi^j = k_{\rm p,dc}(nv_{\rm pv} - v^j_{\rm dc}) + k_{\rm i,dc}\int (nv_{\rm pv} - v^j_{\rm dc})dt. \quad (1)$$

The controller gains $k_{\rm p,dc}$ and $k_{\rm i,dc}$ are chosen to ensure that the floating dc-link control loop is the fastest subsystem such that its dynamics are invisible to the other control loops in Fig. 2.

2) Three Single Phase H-bridge: We consider a three-phase grid voltage of the form

$$\begin{bmatrix} v^{\rm a}_{\rm g} \\ v^{\rm b}_{\rm g} \\ v^{\rm c}_{\rm g} \end{bmatrix} = \begin{bmatrix} V_{\rm g}\cos(\theta_{\rm g}) \\ V_{\rm g}\cos\left(\theta_{\rm g} - \frac{2\pi}{3}\right) \\ V_{\rm g}\cos\left(\theta_{\rm g} - \frac{4\pi}{3}\right) \end{bmatrix}, \quad (2)$$

where $V_{\rm g}$ is the nominal peak grid voltage and $\theta_{\rm g} = \int_0^t \omega_{\rm g} d\sigma$ is the instantaneous grid angle. The set of three H-bridges at the output of the floating dc-link capacitors is connected to the three-phase grid through a line whose inductance and resistance is $L_{\rm f}$ and $R_{\rm f}$ respectively.

The H-bridges are modulated by a dispatchable virtual oscillator controller (dVOC) [12] as follows:

$$\dot{V} = \mu V\left(V_{\rm g}^2 - V^2\right) - \frac{2\eta}{3V}(Q - Q^\star), \quad (3)$$

$$\dot{\theta} = \omega = \omega_0 - \frac{2\eta}{3V^2}(P - P^\star), \quad (4)$$

where the active and reactive power delivered by the module is denoted by P and Q respectively. Controller gains μ and η are selected to implement a nonlinear volt-Var and frequency-watt droop [13]. The voltage at the output of the three inverters are modulated as

$$\begin{bmatrix} v^{\rm a} \\ v^{\rm b} \\ v^{\rm c} \end{bmatrix} = \begin{bmatrix} V\cos(\theta) \\ V\cos\left(\theta - \frac{2\pi}{3}\right) \\ V\cos\left(\theta - \frac{4\pi}{3}\right) \end{bmatrix}. \quad (5)$$

To simplify our analysis, we set the reactive power set-point $Q^\star$ to be zero and define the relative angle between the inverter and grid, $\theta - \theta_{\rm g}$, equal to δ.

The angular dynamics of (4) in terms of δ becomes

$$\dot{\delta} = -\frac{2\eta}{3V^2}(P - P^\star). \quad (6)$$

We now use two assumptions: first, the line connecting the inverter to the grid is predominantly inductive such that $L_{\rm f}\omega \gg R_{\rm f}$. Additionally, the angle δ at rated power is sufficiently small which allows us to approximate $\sin\delta \approx \delta$ to obtain the active power delivered to the grid as

$$P = \frac{3VV_{\rm g}\delta}{2L_{\rm f}\omega}.$$

We take a time derivative on both sides of the preceding equation and substitute for $\dot{\delta}$ in (6) to obtain

$$\frac{2L_{\rm f}\omega}{3VV_{\rm g}}\dot{P} = -\frac{2\eta}{3V^2}(P - P^\star). \quad (7)$$

A properly selected value of μ ensures tight voltage regulation such that $V \approx V_{\rm g}$. This simplifies (7) as

$$\frac{1}{\omega_{\rm P}}\dot{P} := \frac{L_{\rm f}\omega}{\eta}\dot{P} = -P + P^\star. \quad (8)$$

Taking a Laplace transform on both sides yields a first-order plant transfer function of the power control loop as follows:

$$P = \frac{\omega_{\rm P}}{s + \omega_{\rm P}}P^\star. \quad (9)$$

A similar analysis can be carried out for any candidate power converter to obtain an equivalent first-order transfer function for the power control loop.

3) MPPT Controller: The MPPT controller leverages the concavity of a typical PV power-voltage curve to reach the MPP. At MPP, the derivative of PV power, $P_{\rm pv}$, with respect to PV voltage, $v_{\rm pv}$, is zero. We use this property to formulate an integral control law [14] given by

$$v^\star_{\rm pv} = \gamma\int (\partial P_{\rm pv}/\partial v_{\rm pv})dt, \quad (10)$$

where $v^\star_{\rm pv}$ forms the reference for the PV dc-link controller. A linear approximation of the PV plant obtained around the MPP is given by

$$i_{\rm pv} = I_{\rm mpp} - \frac{1}{R_{\rm mpp}}(v_{\rm pv} - V_{\rm mpp}). \quad (11)$$

We differentiate (10) with respect to time and substitute $i_{\rm pv}$ from (11) to obtain

$$\begin{aligned}\dot{v}^\star_{\rm pv} &= \gamma\frac{\partial(v_{\rm pv}i_{\rm pv})}{\partial v_{\rm pv}} = \gamma(v_{\rm pv}\frac{\partial(i_{\rm pv})}{\partial v_{\rm pv}} + i_{\rm pv}),\\ &= -2\frac{\gamma}{R_{\rm mpp}}v_{\rm pv} + 2\gamma I_{\rm mpp}.\end{aligned}$$

Since the PV dc-link controller works on a faster timescale, we substitute $v_{\rm pv} = v^\star_{\rm pv}$ to obtain the following equivalent first-order transfer function of the MPPT loop:

$$\dot{v}^\star_{\rm pv} = \underbrace{-2\frac{\gamma}{R_{\rm mpp}}}_{\omega_{\rm mppt}}v^\star_{\rm pv} + 2\gamma I_{\rm mpp} \quad (12)$$

Having modeled the MPPT control loop and the ac-side power sharing loop with closed form expressions of their respective bandwidths, we shift our focus towards the main contribution of the paper – the PV dc-link control.

III. PV DC-LINK CONTROL

As shown in Fig.1, the dc-link capacitance, $C_{\rm pv}$, acts as an energy buffer between the input PV power, $P_{\rm pv}$ and the output power at the converter terminals, P. The dynamics of the dc-link voltage, $v_{\rm pv}$, is

$$\frac{d}{dt}\left(\frac{1}{2}C_{\rm pv}v^2_{\rm pv}\right) = P_{\rm pv} - P = v_{\rm pv}\,i_{\rm pv} - P$$

This report is available at no cost from the National Renewable Energy Laboratory at www.nrel.gov/publications.

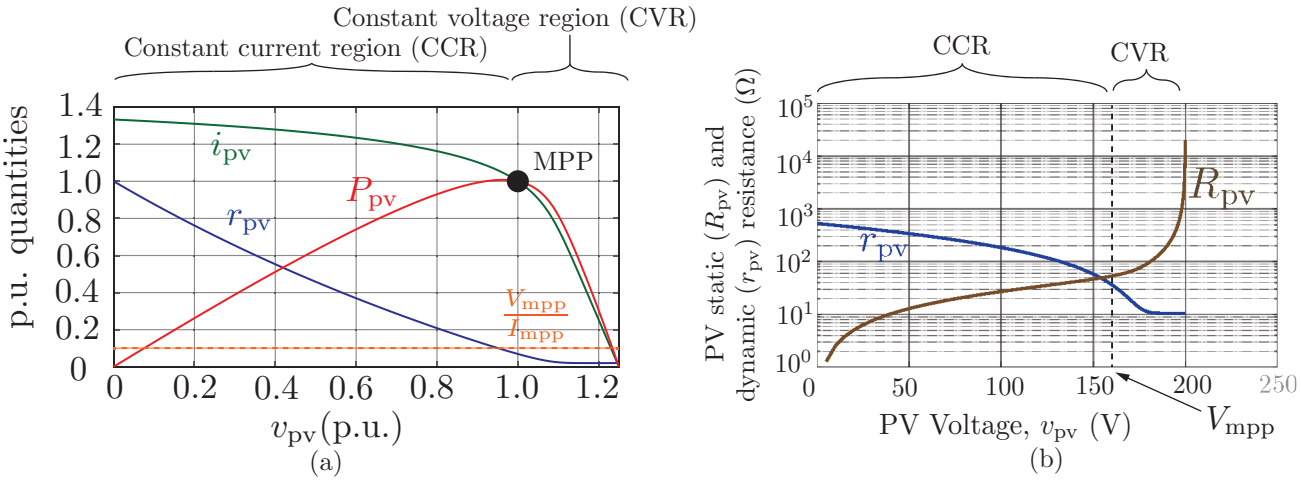

Fig. 3: The static and dynamic characteristics of a PV module. The plot in (a) shows per-unitized voltage, current, and power with respect to their MPP values, whereas r_{pv} is scaled by its maximum value, $r_{pv,max}$. In the same plot $R_{mpp} = V_{mpp}/I_{mpp}$ is scaled by $r_{pv,max}$ and is shown to intersect r_{pv} near the MPP. The absolute values of large and small signal resistances are plotted in (b) to demarcate the different regions of the PV curve.

$$C_{pv} v_{pv} \frac{dv_{pv}}{dt} = v_{pv} i_{pv} - P. \tag{13}$$

We implement the following PI controller to regulate v_{pv} towards the reference, $v_{pv}^{\star}$:

$$P^{\star} = k_p (v_{pv} - v_{pv}^{\star}) + k_i \int (v_{pv} - v_{pv}^{\star}) dt, \tag{14}$$

where the $P^{\star}$ is the output power reference for the downstream converter.

A. Conventional Modeling and Design

1) Modeling: An exact representation of the the PV current in terms of its physical parameters [2] is given by

$$i_{pv} = i_o - i_{sat}\left(e^{\frac{v_{pv}+i_{pv}R_s}{aV_T}} - 1\right), \tag{15}$$

where i_o is the photocurrent generated due to incident sunlight, i_{sat} is the diode saturation current, and R_s is the series equivalent resistance. V_T is the thermal equivalent voltage and a is the diode-ideality constant. In the conventional approach [3], a linear approximation of the PV plant is obtained only around the MPP as follows:

$$i_{pv} = I_{mpp} - \beta(v_{pv} - V_{mpp}), \tag{16}$$

where V_{mpp} and I_{mpp} are the voltage and current at the MPP and β is approximated as

$$\beta = \left.\frac{\partial i_{pv}}{\partial v_{pv}}\right|_{v_{pv}=V_{mpp}} \approx \frac{I_{mpp}}{V_{mpp}}.$$

Around the nominal point $v_{pv} = V_{mpp}$, (13) reduces to

$$C_{pv} \frac{d}{dt} v_{pv} = i_{pv} - \frac{P^{\star}}{V_{mpp}}.$$

Substitution of (16) yields

$$C_{pv} \frac{d}{dt} v_{pv} = I_{mpp} - \beta(v_{pv} - V_{mpp}) - \frac{P^{\star}}{V_{mpp}}.$$

Taking the Laplace transform of both sides of the equation yields

$$v_{pv}(s) = \underbrace{\frac{I_{mpp} + \beta V_{mpp}}{sC_{pv} + \beta}}_{Disturbance} - \underbrace{\frac{P^{\star}/V_{mpp}}{sC_{pv} + \beta}}_{Control}. \tag{17}$$

2) Controller Design: We implement the plant-inversion method [15] on (17) to obtain the PI controller gains

$$k_p = \omega_{pv} V_{mpp} C_{pv}, \qquad k_i = \omega_{pv} V_{mpp} \beta. \tag{18}$$

3) Stability Criteria: To ensure stable operation, the bandwidths are separated in the timescale as follows:

$$\omega_{mppt} \ll \omega_{pv} \ll \omega_P$$

We substitute the bandwidths from (8)–(12) to obtain

$$\frac{2\gamma}{R_{mpp}} \ll \omega_{pv} \ll \frac{\eta}{L_f \omega}, \tag{19}$$

where ω_{pv} satisfies (19).

B. Proposed Modeling and Design Approach

1) Modeling: The conventional PV model in (15) presents two important caveats. First, the transcendental equation (15) for i_{pv} is itself a function of i_{pv}, as a result of which a solution of i_{pv} for small-signal analysis is elusive. Additionally, the parameters described in (15) are not readily available from PV manuals. On the contrary, the model in [16] specifies the PV voltage, v_{pv}, exclusively in terms of the commonly available PV parameters- V_{oc}, I_{sc}, V_{mpp}, and I_{mpp}. The relationship between v_{pv} and i_{pv} is given by

$$v_{pv} = \frac{\frac{V_{oc} \ln\left(2 - \left(\frac{i_{pv}}{I_{sc}}\right)^N\right)}{\ln(2)} - R_s(i_{pv} - I_{sc})}{1 + \frac{R_s I_{sc}}{V_{oc}}}, \tag{23}$$

where the additional parameters, R_s, N, and α [16] depend exclusively on V_{oc}, I_{sc}, V_{mpp}, and I_{mpp}. We use the aforementioned model to define the new small signal PV resistance,

This report is available at no cost from the National Renewable Energy Laboratory at www.nrel.gov/publications.

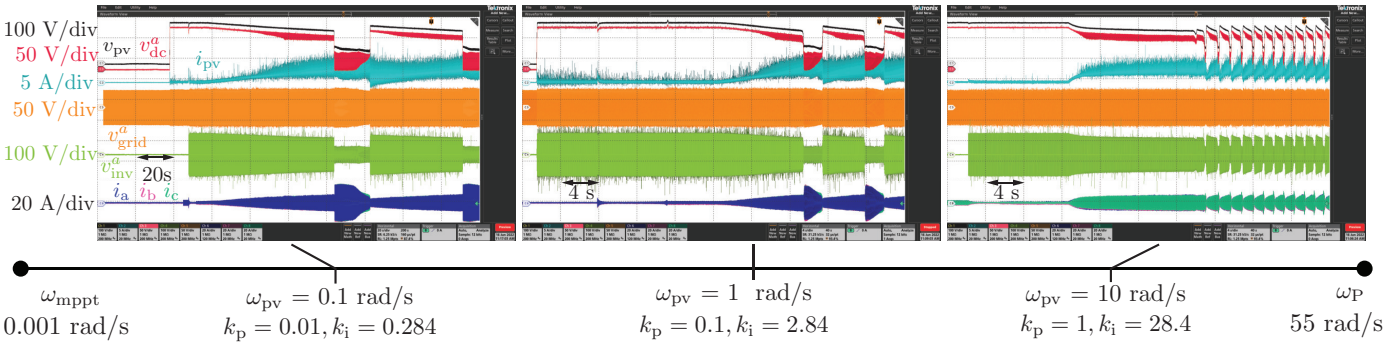

Fig. 4: Experimental results show the PV voltage, PV current, phase-a inverter switched voltage, phase-a grid voltage, and the three phase ac currents when controllers are designed with conventional timescale separation and linearization around the MPP. The waveforms illustrate instabilities during the transition from MPP to constant-current region for three sets of controllers whose bandwidths are intermediate to the faster power controller and slower MPPT controller.

r_{pv}, as

$$r_{\text{pv}} := -\frac{\partial v_{\text{pv}}}{\partial i_{\text{pv}}} = \frac{\frac{V_{\text{mpp}}-V_{\text{oc}}}{I_{\text{mpp}}} + \frac{V_{\text{oc}}\rho\left(\frac{i_{\text{pv}}}{I_{\text{sc}}}\right)^{\gamma-1}\kappa_1}{I_{\text{sc}}\log\left(\frac{I_{\text{mpp}}}{I_{\text{sc}}}\right)\left(\left(\frac{i_{\text{pv}}}{I_{\text{sc}}}\right)^{\gamma}-2\right)\kappa_2}}{\frac{I_{\text{sc}}(V_{\text{mpp}}-V_{\text{oc}})}{I_{\text{mpp}}V_{\text{oc}}} - 1}, \tag{24}$$

where the quantities γ, ρ, κ_1, and κ_2 are given by

$$\gamma = \log\left(2 - \frac{1}{2\frac{V_{\text{mpp}}\left(\frac{I_{\text{sc}}(V_{\text{mpp}}-V_{\text{oc}})}{I_{\text{mpp}}V_{\text{oc}}}-1\right)+\frac{(I_{\text{mpp}}-I_{\text{sc}})(V_{\text{mpp}}-V_{\text{oc}})}{I_{\text{mpp}}}}{V_{\text{oc}}}}\right),$$

$$\rho = \frac{\gamma}{\log\left(\frac{I_{\text{mpp}}}{I_{\text{sc}}}\right)}, \quad \kappa_1 = 9.007\times10^{15}, \kappa_2 = 6.243\times10^{15}.$$

The constants κ_1, κ_2 are universal for any PV module. The model described by (23) is plotted in Fig. 3(a) to accurately capture the PV characteristics. In Fig. 3(b), we plot the large-signal PV resistance, denoted by $R_{\text{pv}} := V_{\text{pv}}/I_{\text{pv}}$, and r_{pv} appearing in (24).

In the constant current (voltage) region, the small-signal resistance is larger (smaller) than the corresponding large-signal resistance. Whereas around the MPP, the two resistances have comparable values. We will subsequently use these three regions and the values of their corresponding small- and large-signal resistances to analyse and design the PV dc-link controller.

To include the small-signal PV resistance, we perturb the nonlinear dynamics of the capacitor voltage in (13) around a nominal operating point to obtain

$$\begin{aligned} &C_{\text{pv}}(V_{\text{pv}}+\widetilde{v}_{\text{pv}})\frac{d}{dt}(V_{\text{pv}}+\widetilde{v}_{\text{pv}}) \\ &\quad = (V_{\text{pv}}+\widetilde{v}_{\text{pv}})(I_{\text{pv}}+\widetilde{i}_{\text{pv}}) - (P^\star+\widetilde{p}^\star). \end{aligned}$$

The large-signal terms balance themselves and are removed from both sides of the preceding equation to obtain the following [7] nonlinear small-signal model:

$$C_{\text{pv}}V_{\text{pv}}\frac{d}{dt}(\widetilde{v}_{\text{pv}}) = I_{\text{pv}}\widetilde{v}_{\text{pv}} + V_{\text{pv}}\widetilde{i}_{\text{pv}} + \widetilde{v}_{\text{pv}}\widetilde{i}_{\text{pv}} - \widetilde{p}^\star \tag{25}$$

Substitute the definition of r_{pv} from (24) into (25) to obtain

$$\begin{aligned} C_{\text{pv}}V_{\text{pv}}\frac{d}{dt}(\widetilde{v}_{\text{pv}}) &= \widetilde{v}_{\text{pv}}\frac{V_{\text{pv}}}{R_{\text{pv}}} + V_{\text{pv}}\frac{-1}{r_{\text{pv}}}\widetilde{v}_{\text{pv}} + \widetilde{v}_{\text{pv}}\frac{-1}{r_{\text{pv}}}\widetilde{v}_{\text{pv}} - \widetilde{p}^\star \\ &= V_{\text{pv}}\left(\frac{1}{R_{\text{pv}}} - \frac{1}{r_{\text{pv}}}\right)\widetilde{v}_{\text{pv}} - \frac{1}{r_{\text{pv}}}\widetilde{v}_{\text{pv}}^2 - \widetilde{p}^\star. \end{aligned}$$

The small-signal power reference, $\widetilde{p}^\star$, obtained by linearizing (14) around the nominal operating point is

$$\widetilde{p}^\star = k_p(\widetilde{v}_{\text{pv}} - \widetilde{v}^\star_{\text{pv}}) + \widetilde{x}_{\text{pv}},$$

where the integral state variable x_{pv} is defined as

$$\dot{x}_{\text{pv}} = k_{\text{i}}(v_{\text{pv}} - v^\star_{\text{pv}}).$$

We compose the small signal state vector $y = [\widetilde{v}_{\text{pv}}, \widetilde{x}_{\text{pv}}]^\top$ whose dynamics are given by $\dot{y} = f(y, \widetilde{v}^\star_{\text{pv}})$, where the flow

$$\frac{d\widetilde{v}_{\text{pv}}}{dt} = \frac{1}{C_{\text{pv}}}\left(\frac{1}{R_{\text{pv}}} - \frac{1}{r_{\text{pv}}}\right)\widetilde{v}_{\text{pv}} - \frac{1}{C_{\text{pv}}V_{\text{pv}}r_{\text{pv}}}\widetilde{v}_{\text{pv}}^2 - \frac{1}{C_{\text{pv}}V_{\text{pv}}}\left(k_p(\widetilde{v}_{\text{pv}} - \widetilde{v}^\star_{\text{pv}}) + \widetilde{x}_{\text{pv}}\right) =: f_1, \tag{20}$$

$$\frac{d\widetilde{x}_{\text{pv}}}{dt} = k_i(\widetilde{v}_{\text{pv}} - \widetilde{v}^\star_{\text{pv}}) =: f_2 \tag{21}$$

$$\begin{aligned} \dot{\mathcal{V}} = \widetilde{v}_{\text{pv}}\dot{\widetilde{v}}_{\text{pv}} + \widetilde{x}_{\text{pv}}\dot{\widetilde{x}}_{\text{pv}} &= \frac{1}{C_{\text{pv}}}\left(\frac{1}{R_{\text{pv}}} - \frac{1}{r_{\text{pv}}}\right)\widetilde{v}_{\text{pv}}^2 - \frac{1}{C_{\text{pv}}V_{\text{pv}}r_{\text{pv}}}\widetilde{v}_{\text{pv}}^3 - \frac{1}{C_{\text{pv}}V_{\text{pv}}}\left(k_p\widetilde{v}_{\text{pv}}^2 + \widetilde{x}_{\text{pv}}\widetilde{v}_{\text{pv}}\right) + k_i\widetilde{x}_{\text{pv}}\widetilde{v}_{\text{pv}} \\ &= \underbrace{\left(\frac{1}{C_{\text{pv}}}\left(\frac{1}{R_{\text{pv}}} - \frac{1}{r_{\text{pv}}}\right) - \frac{k_{\text{p}}}{C_{\text{pv}}V_{\text{pv}}}\right)\widetilde{v}_{\text{pv}}^2 - \frac{1}{C_{\text{pv}}V_{\text{pv}}r_{\text{pv}}}\widetilde{v}_{\text{pv}}^3}_{:=g_1(\widetilde{v}_{\text{pv}})} + \widetilde{x}_{\text{pv}}\widetilde{v}_{\text{pv}}\underbrace{\left(k_{\text{i}} - \frac{1}{C_{\text{pv}}V_{\text{pv}}}\right)}_{g_2}. \end{aligned} \tag{22}$$

This report is available at no cost from the National Renewable Energy Laboratory at www.nrel.gov/publications.

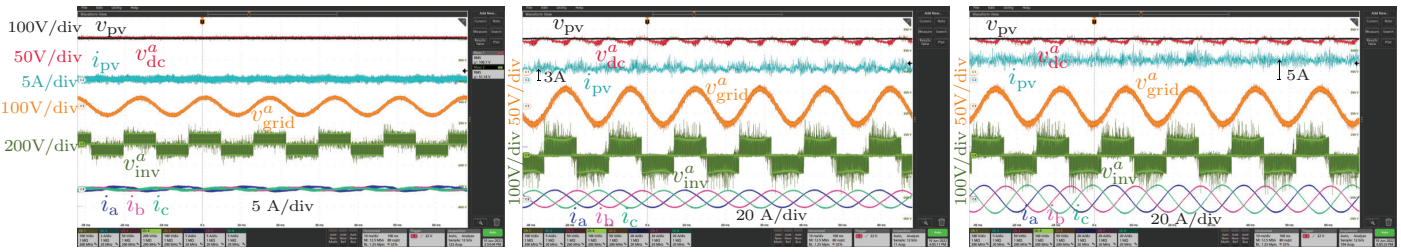

Fig. 5: Experimental results illustrate the dc- and ac-side quantities zoomed in on a few ac cycles for controllers designed with Lyapunov analysis for the proposed PV model. In (a) we observe the start-up at open-circuit condition. MPPT operation at MPP_a and MPP_b are shown in (b) and (c) respectively.

vector $f := [f_1, f_2]^\top$ is expanded in (20) and (21). Without loss of generality, we analyze the stability of the system $\dot{y} = f(y, v^\star_{\text{pv}})$ at zero input such that $\widetilde{v}^\star_{\text{pv}} = 0$. Assuming $f := [f_1, f_2]^\top$ is locally Lipschitz, we choose a positive definite Lyapunov candidate, $\mathcal{V} = 0.5(\widetilde{v}^2_{\text{pv}} + \widetilde{x}^2_{\text{pv}})$ to analyze the stability of the PV dc-link control. In (22) we obtain the derivative of $\mathcal{V}$ along the trajectory of the system $\dot{y} = f(y)$.

2) Controller Design: To ensure asymptotic stability, we require a strictly negative derivative of the Lyapunov candidate such that $\dot{\mathcal{V}} < 0$. Since the product of states $\widetilde{v}_{\text{pv}}\widetilde{x}_{\text{pv}}$ does not guarantee strict negativity, we set its coefficient in (22) to zero. This gives our first design equation: $k_\text{i} = 1/(C_{\text{pv}}V_{\text{pv}})$. To design a fixed controller gain that does not vary with the operating voltage, we set $V_{\text{pv}} = V_{\text{mpp}}$. The controller gain, k_i, is obtained as

$$k_\text{i} = 1/(C_{\text{pv}}V_{\text{mpp}}). \tag{26}$$

Next, we simplify $\dot{\mathcal{V}}$ by observing the relationship between R_{pv} and r_{pv} in different regions of the PV curve as shown in Figure 3(b). The three distinct regions of operation: constant current region (CCR), MPP region, and constant voltage region (CVR) yield

$$\begin{aligned} &r_{\text{pv}} \gg R_{\text{pv}} \qquad \text{in CCR,} \\ &r_{\text{pv}} \approx R_{\text{pv}} \approx R_{\text{mpp}} \qquad \text{around MPP,} \\ &r_{\text{pv}} \ll R_{\text{pv}} \qquad \text{in CVR.} \end{aligned} \tag{27}$$

The relationship between r_{pv} and R_{pv} from (27) is substituted into $g_1(\widetilde{v}_{\text{pv}})$ in (22) to simplify $\dot{\mathcal{V}}$ as

$$\begin{aligned} \dot{\mathcal{V}} &= \frac{1}{C_{\text{pv}}V_{\text{pv}}}(I_{\text{pv}} - k_p)\widetilde{v}^2_{\text{pv}} \qquad \text{in CCR,} \\ &= -\frac{1}{C_{\text{pv}}V_{\text{pv}}}\left(\frac{\widetilde{v}_{\text{pv}}}{R_{\text{mpp}}} + k_\text{p}\right)\widetilde{v}^2_{\text{pv}} \qquad \text{around MPP,} \\ &= -\frac{1}{C_{\text{pv}}V_{\text{pv}}}(k_\text{p} + \frac{V_{\text{pv}}}{r_{\text{pv}}})\widetilde{v}^2_{\text{pv}} \qquad \text{in CVR.} \end{aligned} \tag{28}$$

3) Stability Criteria: It is readily seen from (28) that for a non-negative k_p stability is always guaranteed in CVR. Stability is further guaranteed in CCR if

$$k_\text{p} > I_{\text{pv}}, \tag{29}$$

where the maximum value of I_{pv} is I_{sc}. Stability can only be guaranteed locally around the MPP. Since $\dot{\mathcal{V}} = -(k_\text{p} + \widetilde{v}_{\text{pv}}/R_{\text{pv}})\widetilde{v}^2_{\text{pv}}$, a large value of k_p ensures a larger region of attraction. The concavity of the PV curve and the relatively tight MPP range guarantees that when larger oscillations cause operating point swings, it is quickly pushed into the CCR or CVR. Since both CCR and CVR are stable under the assumption of $k_\text{p} > I_{\text{sc}}$, the MPP point, and hence the whole system, is also rendered stable.

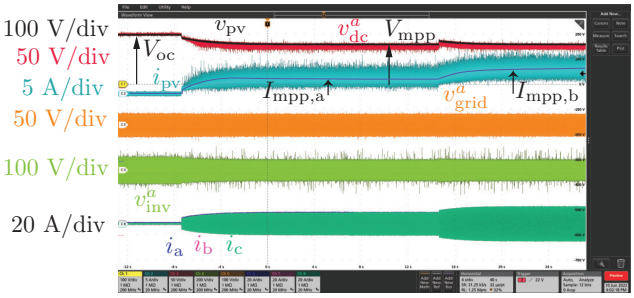

Fig. 6: Experimental waveforms capture the dc- and ac-side quantities for controllers designed based on Lyapunov theory for the proposed PV model as the PV panel moves from open-circuit condition to MPP_a and MPP_b without any instabilities.

TABLE I
SYSTEM PARAMETERS.

	Symbol	Description	Value	Units
Ac system	S_{rated}	module VA rating	1000	VA
	$f_{\text{sw,i}}$	inverter switching frequency	10	kHz
	V_g	rms line-neutral grid voltage	30	V
	ω_{nom}	rated frequency	60	Hz
	L_f	inductance	4.8	mH
	R_f	resistance	0.8	Ω
	μ	dVOC controller gain 1	1	$\text{V}^{-2}s^{-1}$
	η	dVOC controller gain 2	100	$\Omega\ \text{s}^{-1}$
MPPT & PV	C_{pv}	PV input capacitance	660	μF
	V_{oc}	open- circuit voltage	200	V
	$I_{\text{sc,a}}$	short- circuit current at MPP_a	4.0	A
	$I_{\text{sc,b}}$	short- circuit current at MPP_b	6.0	A
	V_{mpp}	MPP voltage at MPP_a, MPP_b	160	V
	$I_{\text{mpp,a}}$	MPP current at MPP_a	3.0	A
	$I_{\text{mpp,b}}$	MPP current at MPP_b	5.0	A
	k_p	proportional gain	10	A
	k_i	integral gain	9.47	As^{-1}
	γ	MPPT gain	0.0533	$\Omega\ \text{s}^{-1}$

This report is available at no cost from the National Renewable Energy Laboratory at www.nrel.gov/publications.

IV. Experimental Results

The QAB-based dc to three-phase ac converter shown in Fig. 2 is used to validate the proposed control approach. At the dc input of the QAB, a Solar Array Simulator (SAS) emulates the following PV curve: $V_{\rm mpp} = 160{\rm V}, V_{\rm oc} = 200{\rm V}, I_{\rm mpp} = 3{\rm A}, I_{\rm sc} = 4{\rm A}$. We will refer to this curve as $\text{MPP}_{\rm a}$. To study the robustness of the proposed controller against varying insolation, we switch between $\text{MPP}_{\rm a}$ and $\text{MPP}_{\rm b}$, where the latter is the PV curve corresponding to $V_{\rm mpp} = 160{\rm V}, V_{\rm oc} = 200{\rm V}, I_{\rm mpp} = 5{\rm A}$, and $I_{\rm sc} = 6{\rm A}$.

A. Experimental Results with Conventional Controllers

Fig. 4 shows the experimental results with the conventional controller. We show three sets of controllers designed via timescale separation based on the conventional model of (17). Three dc-link control bandwidths of 0.1 rad/s, 1.0 rad/s, and 10 rad/s are accommodated between the faster power controller of bandwidth $\omega_{\rm P} = \eta/X_{\rm f} = 55$ rad/s, and the slower MPPT controller of bandwidth $\omega_{\rm mppt} = 2\gamma/R_{\rm mpp} = 0.001$ rad/s. We observe that for each set of controllers, the transition from the open-circuit condition to MPP is stable. Instability sets in when the oscillations around the MPP push PV operation into the CCR, after which the converter is no longer able to achieve stable operation. This matches well with our Lyapunov analysis where the three controllers are designed via timescale separation such that $k_{\rm p} < I_{\rm pv}$ violates the stability constraint of (29).

B. Experimental Results with Proposed Controller

MPPT operation with the proposed controller is shown in Fig. 6. We choose $k_{\rm p} = 10\,A$ to satisfy (29) when the short-circuit currents at $\text{MPP}_{\rm a}$ and $\text{MPP}_{\rm b}$ are 4 A and 6 A respectively. Similarly for $V_{\rm mpp} = 160\,{\rm V}$, we choose $k_{\rm i} = 9.47\,{\rm As}^{-1}$ to satisfy (26). For exact comparison with the controller obtained by conventional design, $\omega_{\rm mppt}$ and $\omega_{\rm P}$ are kept identical. The proposed controller is able to reach $\text{MPP}_{\rm a}$ with stable operation at the MPP. To test the robustness of the proposed strategy, the insolation of the PV simulator is abruptly changed to emulate $\text{MPP}_{\rm b}$. The proposed controller is able to ride-through the transient and reach $\text{MPP}_{\rm b}$ with stable power dispatch at the new operating point.

We focus on the steady-state performance of the proposed controller in Fig. 5 over a few ac cycles. In Fig.5(a) we capture the initial steady-state where the inverter switched output voltage for the phase-a, $v^a_{\rm inv}$, is exactly synchronized to the corresponding grid voltage, $v^a_{\rm grid}$. Steady state operation at $\text{MPP}_{\rm a}$ is shown in Fig. 5(b) where the inverter switched voltage, $v^a_{\rm inv}$, is phase-shifted from the grid-voltage, $v^a_{\rm grid}$, to extract approximately 480 W of solar power. Similarly, stable operation is shown with greater phase-shift and higher ac-side currents in Fig. 5(c) where the converter ensures smooth operation at $\text{MPP}_{\rm b}$.

V. Conclusion

In this paper, we proposed a generalized technique for the design of control loops in PV-connected converters. A nonlinear small-signal model of the PV module was developed that relies exclusively on datasheet parameters ($V_{\rm mpp}, I_{\rm mpp}, V_{\rm oc}, I_{\rm sc}$). A Lyapunov-based approach was used to analyse and design the PV dc-link controller. We uncovered new stability conditions that are absent from conventional timescale-separation-based design techniques. The proposed design technique is validated experimentally and results illustrate the criticality of the stability conditions obtained from Lyapunov analysis.

References

[1] I. Verbytskyi, M. Lukianov, K. Nassereddine, B. Pakhaliuk, O. Husev, and R. M. Strzelecki, "Power converter solutions for industrial PV applications - a review," *Energies*, vol. 15, no. 9, 2022.

[2] M. G. Villalva, J. R. Gazoli, and E. R. Filho, "Comprehensive approach to modeling and simulation of photovoltaic arrays," *IEEE Transactions on Power Electronics*, vol. 24, no. 5, pp. 1198–1208, 2009.

[3] S. Maity and P. K. Sahu, "Modeling and analysis of a fast and robust module-integrated analog photovoltaic MPP tracker," *IEEE Transactions on Power Electronics*, vol. 31, no. 1, pp. 280–291, 2016.

[4] A. Mäki, S. Valkealahti, and T. Suntio, "Dynamic terminal characteristics of a photovoltaic generator," in *Proceedings of 14th International Power Electronics and Motion Control Conference EPE-PEMC 2010*, pp. T12–76–T12–80, 2010.

[5] T. Messo, J. Puukko, and T. Suntio, "Effect of MPP-tracking DC/DC converter on VSI-based photovoltaic inverter dynamics," in *6th IET International Conference on Power Electronics, Machines and Drives (PEMD 2012)*, pp. 1–6, 2012.

[6] T. Suntio, J. Leppäaho, J. Huusari, and L. Nousiainen, "Issues on solar-generator interfacing with current-fed MPP-tracking converters," *IEEE Transactions on Power Electronics*, vol. 25, no. 9, pp. 2409–2419, 2010.

[7] L. Nousiainen, J. Puukko, A. Mäki, T. Messo, J. Huusari, J. Jokipii, J. Viinamäki, D. T. Lobera, S. Valkealahti, and T. Suntio, "Photovoltaic generator as an input source for power electronic converters," *IEEE Transactions on Power Electronics*, vol. 28, no. 6, pp. 3028–3038, 2013.

[8] J. Puukko, T. Messo, and T. Suntio, "Effect of photovoltaic generator on a typical VSI-based three-phase grid-connected photovoltaic inverter dynamics," in *IET Conference on Renewable Power Generation (RPG 2011)*, pp. 1–6, 2011.

[9] L. Callegaro, M. Ciobotaru, D. J. Pagano, and J. E. Fletcher, "Feedback linearization control in photovoltaic module integrated converters," *IEEE Transactions on Power Electronics*, vol. 34, no. 7, pp. 6876–6889, 2019.

[10] B. Pawar, E. I. Batzelis, S. Chakrabarti, and B. C. Pal, "Grid-forming control for solar PV systems with power reserves," *IEEE Transactions on Sustainable Energy*, vol. 12, no. 4, pp. 1947–1959, 2021.

[11] P. K. Achanta, B. B. Johnson, G.-S. Seo, and D. Maksimovic, "A multilevel DC to three-phase AC architecture for photovoltaic power plants," *IEEE Transactions on Energy Conversion*, vol. 34, no. 1, pp. 181–190, 2019.

[12] M. Lu, R. Mallik, B. Johnson, and S. Dhople, "Dispatchable virtual-oscillator-controlled inverters with current-limiting and MPPT capabilities," in *2021 IEEE Energy Conversion Congress and Exposition (ECCE)*, pp. 3316–3323, 2021.

[13] M. Lu, S. Dutta, V. Purba, S. Dhople, and B. Johnson, "A grid-compatible virtual oscillator controller: Analysis and design," in *2019 IEEE Energy Conversion Congress and Exposition (ECCE)*, pp. 2643–2649, Sep. 2019.

[14] T. Esram and P. L. Chapman, "Comparison of photovoltaic array maximum power point tracking techniques," *IEEE Transactions on Energy Conversion*, vol. 22, no. 2, pp. 439–449, 2007.

[15] T. A. Doyle J., Francis B., *Feedback Control Theory*. Wiley, 2nd ed., 2008.

[16] L. Britton and Tanju, "A 9 kW high-performance solar array simulator," vol. SA WPP-054, pp. 2643–2649, Aug. 1993.

This report is available at no cost from the National Renewable Energy Laboratory at www.nrel.gov/publications.